One-Step Synthesis of Nanostructured Cu−Mn/TiO$_2$ via Flame Spray Pyrolysis: Application to Catalytic Combustion of CO and CH$_4$

Xing Yuan,[†] Menglei Qing,[†] Lingquan Meng, and Haibo Zhao*

ACCESS | 📊 Metrics & More | 📖 Article Recommendations

ABSTRACT: Catalytic combustion has been widely applied to remove the trace combustible pollutants. However, the earth-abundant and high-performance nanocatalysts are still the main research focus on promoting catalytic efficiency. Herein, the Cu and Mn mixed oxides supported on TiO$_2$ nanoparticles with various Cu and Mn molar contents synthesized via the flame spray pyrolysis (FSP) technique are utilized in the catalytic oxidation of lean CO and CH$_4$. Initially, the Cu−Mn/TiO$_2$ nanocatalysts are composed of spherical structures with a diameter of about 20 nm, whose specific surface area is between 60 and 90 m^2/g. The Cu element is more evenly distributed on the TiO$_2$ surface than the Mn element, owing to the distinctly different ion radii. Both the copper and manganese cations could incorporate into the TiO$_2$ lattice, which generates oxygen vacancies and enhances the diffusion of oxygen ions, causing the transformation of the antanse to rutile phase. When the molar content of the Cu−Mn increases to less than 30 mol %, the temperature of its reduction peak keeps decreasing due to the hydrogen spillover effect. Moreover, the catalytic performances of the Cu−Mn/TiO$_2$ with 12 mol % loading (12CMT) are all optimal during the low-temperature and the high-temperature stages, which are superior to the FSP-made copper manganese or copper titanium oxides. This is attributed to the small crystal particles, highly dispersed active components of CuO$_x$ and MnO$_x$, and the higher ratios of Cu^{1+}/Cu and Mn^{4+}−O$_{ads}$ Lewis acid−base pairs. In addition, the strong interaction between Cu−Mn components and rutile phase support can tremendously promote the activity of catalytic combustion. Under the simulated flue gas, the catalytic properties of 12CMT decreases in comparison with those of CO and CH$_4$ mixed gas due to the introduction of CO$_2$. Ultimately, the Cu−Mn/TiO$_2$ samples exhibit the outstanding water resistance, thanks to the hydrophobization of the catalyst surface.

1. INTRODUCTION

The catalytic combustion provides an economical and effective removal approach for CO and CH$_4$ as one of the main sources of air pollution.[1,2] The copper-based and manganese-based catalysts present the outstanding reaction activity for CO and CH$_4$, as well as the low cost, which are expected to replace precious metal catalysts.[3−5] Compared with monometallic nanocatalysts such as a copper oxide or manganese oxide, the bimetallic nanocatalysts of two transition-metal composites are widely used in the field of heterogeneous catalysis, because the synergistic effect between different metal oxides can significantly promote the catalytic activity and recyclability.[6,7] There are a multitude of literature sources about bimetallic nanocatalysts containing Cu and Mn elements for catalytic oxidation. It is well-known that the hopcalite catalyst composed of copper−manganese mixed oxide discovered in 1920 has been commercially applied in numerous industrially significant oxidation reactions.[8,9] Gao et al.[10] doped Cu, Ni, Fe, and Co transition metals in MnO$_2$ to tune the chemical bond of Mn−O and found that copper-doped MnO$_2$ formed more oxygen vacancies to enhance the CO catalytic activity. Biswas et al.[11] fabricated the mesoporous copper oxide supported on MnO$_x$ catalysts and elucidated a synergistic-cooperative effect between the manganese and copper through the role of labile lattice oxygen. Therefore, the Cu−Mn composite oxides have attracted wide attention for catalytic combustion, thanks to low-cost catalytic materials with a high reactivity and easy

fabrication. However, the pure bimetallic nanocatalysts containing Cu and Mn are less stable and active at the high temperature. There is an effective way of providing supports into the catalytic materials for enhancement of thermal stability and activity.[12]

Titanium dioxide TiO$_2$ has been a particularly promising material in various catalytic fields, especially as a catalyst carrier, due to high surface area, outstanding chemical stability, and excellent oxygen storage capacity.[13−15] Moreover, the effect of the strong bimetallic heterogeneous catalysts and TiO$_2$ support interaction is responsible for the high dispersion and remarkable stability of the bimetal supported TiO$_2$ catalysts.[16] Min et al.[17] prepared an ordered mesoporous Cu−Mn/TiO$_2$ heterogeneous catalyst via a wet-impregnation manner and proposed that the mesoporous anatase serves as a stable substrate with a high surface area for Cu−Mn species and a promoter for the synergistic elimination of organic pollutants. Sun et al. reported that CuO−MnO$_x$/TiO$_2$ is more active than single active species, which is ascribed to the
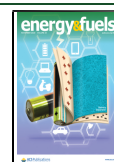
Table 1. Specific Precursor Dosages for the Preparation of Cu−Mn/TiO$_2$

catalyst	solvent	tetrabutyl titanate (mL)	copper acetate (g)	manganese acetate (g)	precursor flow (mL/min)	dispersion flow (L/min)	premixed flame (L/min)
4CMT	ethanol (100 mL)	17.25	0.21	0.26	3	5	0.75(CH_4) 1.5(O_2)
12CMT	ethanol (100 mL)	17.25	0.69	0.84	3	5	0.75(CH_4) 1.5(O_2)
20CMT	ethanol (100 mL)	17.25	1.27	1.54	3	5	0.75(CH_4) 1.5(O_2)
30CMT	ethanol (100 mL)	17.25	2.17	2.65	3	5	0.75(CH_4) 1.5(O_2)
TiO$_2$	ethanol (100 mL)	17.25			3	5	0.75(CH_4) 1.5(O_2)
CuO	ethanol (100 mL)		2.52		3	5	0.75(CH_4) 1.5(O_2)
MnO$_x$	ethanol (100 mL)			3.09	3	5	0.75(CH_4) 1.5(O_2)
CuO−MnO$_x$	ethanol (100 mL)		1.26	1.55	3	5	0.75(CH_4) 1.5(O_2)

generation of the surface synergetic oxygen vacancy between Cu and Mn components.[18] Thus, the Cu and Mn mixed oxides supported on the TiO$_2$ carrier can maintain excellent dispersion and catalytic activity with a remarkable application prospect for catalytic combustion of CO and CH$_4$. Unfortunately, as the content of Mn or Cu exceeds the threshold value of preparation methods, the appearance of large crystalline MnO$_x$ or CuO on support leads to the notorious decrease of the catalytic capability. Hence, the improvement of the Cu or Mn loading without forming large grains on the catalyst surface plays a vital role in combustion oxidation.

Flame spray pyrolysis (FSP) has been applied to the production of the diverse high-performance nanoparticles owing to its mass production, rapid preparation, simplified process design, fabrication, and collection.[19−22] Mädler et al.[23] proved that the FSP technology is an effective method to synthesize single-component and multicomponent nanoparticles with high purity and excellent dispersion. In the synthesis process of FSP, the gas-phase metal precursor mixes at the atomic level to promote the interaction between composite materials.[4,24] Furthermore, the copper or manganese ions in the catalysts via FSP would not spill over to the material surface without the calcination process that brings about a worse instability of the TiO$_2$ crystal structure.[8,25] Although the composite metal oxides synthesized by FSP technologies have been successfully utilized in numerous environments and engineering fields, there are few publications about catalytic combustion of CO and CH$_4$ over the FSP-made Cu−Mn/TiO$_2$ nanoparticles.

This paper reports the Cu−Mn/TiO$_2$ nanocomposites with various Cu and Mn loadings synthesized by FSP, focusing on its physicochemical properties and catalytic performance for oxidation of CO, CH$_4$, (CO + CH$_4$) mixed gas, and simulated flue gas. The phase composition and morphology of materials are characterized by X-ray diffraction (XRD), Brunauer−Emmett−Teller methods (BET), X-ray photoelectron spectroscopy (XPS), transmission electron microscopy (TEM), and H$_2$ temperature-programmed reduction (H$_2$-TPR). The influence of different CuO$_x$ and MnO$_x$ contents on the morphology, structure, and chemical properties of the Cu−Mn/TiO$_2$ samples is comprehensively analyzed for better control of the CO and CH$_4$ pollutant emission.

2. EXPERIMENTAL SECTION

2.1. Catalyst Preparation. In the preparation of the Cu−Mn/TiO$_2$ nanocatalyst, titanium butoxide, copper acetate, and manganese acetate are selected as the corresponding metal precursors of TiO$_2$, CuO$_x$, and MnO$_x$. Ethanol is selected as the precursor solvent due to its low vaporization temperature, sufficient combustion, and less carbon depositions in the combustion process. First, a certain amount of copper(II) acetate monohydrate and manganese acetate tetrahydrate is completely dissolved in ethanol with ultrasonic treatment for 10 min, and then 17.25 mL of tetrabutyl titanate is added. The concentration of metals is kept at 0.5 mol/L, and the molar ratio of Cu and Mn is 1:1; meanwhile, the concentration of CuO$_x$, MnO$_x$, and CuO−MnO$_x$ is kept at 0.125 mol/L. It is worth noting that, to avoid the possible hydrolysis of the Ti precursor, the attained ethanol solution containing Cu and Mn acetate is carefully filtered with a molecular sieve to remove the trace water impurities. The samples with various loadings are named YCMT, including 4CMT (4 mol % Cu−Mn/TiO$_2$), 12CMT (12 mol % Cu−Mn/TiO$_2$), 20CMT (20 mol % Cu−Mn/TiO$_2$), and 30CMT (30 mol % Cu−Mn/TiO$_2$). The molar content Y of Cu−Mn is calculated according to the following formula:

$$Y = \frac{n_{Cu} + n_{Mn}}{n_{Cu} + n_{Mn} + n_{Ti}} \times 100\% \tag{1}$$

where n_{Cu}, n_{Mn}, and n_{Ti} are the molar quantities of the Cu, Mn, and Ti elements, respectively. The detailed ratio of the precursor solution and the synthesis parameters of FSP processes are shown in Table 1.

The Cu−Mn/TiO$_2$ nanocatalysts are prepared on a commercial flame spray pyrolysis preparation system (NPS10, Tethis, Italy) shown in Figure 1. Initially, the mixed precursors are delivered by a high-precision syringe pump into an atomizing capillary tube. Then, the dispersion gas of 5 L/min O$_2$ disperses the solution into small droplets with a 1.5 bar gas pressure drop, under the precursor flow rate of 3 mL/min. A premixed pilot flame that consists of 0.75 L/min methane and 1.5 L/min oxygen ignites the precursor liquid. The metal vapors containing Cu, Ti, and Mn elements are violently mixed at the atomic level in the high-temperature flame zone by the combustion and vaporization of the organic precursor. The primary particles of the trimetallic components are formed by the nucleation and surface growth owing to the supersaturation of the metal vapor. Ultimately, the flame aerosol coalesces and sinters to generate the chemically bonded spherical aggregates and physically bonded loose agglomerates, accompanied by the crystallization and phase transformation. The flame-made powder is collected by a glass fiber filter via the vacuum pump.

2.2. Catalyst Characterization. The Brunauer−Emmett−Teller (BET) methodology is used to calculate the specific surface area (SSA) of catalysts by Micromeritics ASAP 2020. The X-ray diffractometer (XRD) technique determines the crystalline phase by
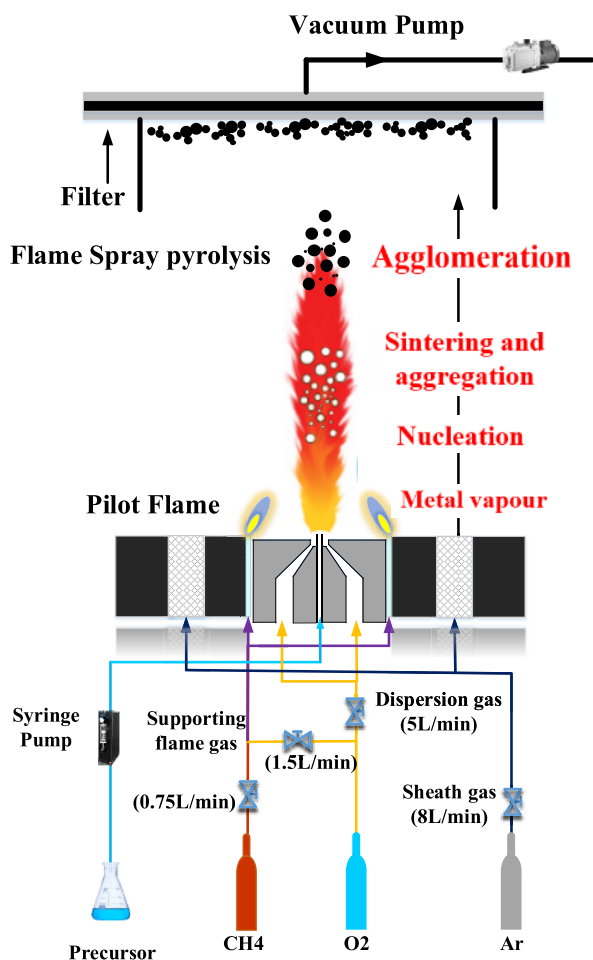
Figure 1. Scheme of the flame spray pyrolysis synthesis apparatus.

PANalytical X'Pert PRO utilizing λ = 1.5406 A Cu Kα radiation. The morphology of trimetallic oxides is observed by a scanning electron microscope (SEM) FEI Siron200 and a transmission electron microscope (TEM) JEOL 2100F with energy-dispersive X-ray spectroscopy (EDX) Apollo XLT SDD. The surface element valence

is analyzed by an X-ray photoelectron spectroscopy (XPS) Thermo ESCALAB 250 utilizing a 1486.6 eV Al Kα radiation with the calibrating binding energy C 1s at 284.6 eV. H$_2$ temperature-programmed reduction (H$_2$-TPR) is conducted out on a fixed-bed tube reactor (i.d. = 8 mm), and the reacted concentration of hydrogen is monitored by a micromeritics AutoChem II-2920. Initially, 0.1 g of fresh catalysts is heated in 100 mL/min N$_2$ from room temperature to 250 °C, holding for 1 h; then, it was cooled to room temperature. Then, a 50 mL/min gas stream of 10 vol % H$_2$/Ar removes N$_2$, holding for 30 min, and the sample is heated at 10 °C/min from room temperature to 650 °C.

2.3. Catalytic Combustion Test. The catalytic oxidation experiments of CO and CH$_4$ are performed in a fixed-bed quartz tube reactor system (i.d. = 8 mm). The catalysts are pretreated and activated in 50 mL/min N$_2$ for 1 h at 120 °C. The catalytic activity of the single CO or CH$_4$ is evaluated by the gaseous mixture of 2 vol % CO or 2 vol % CH$_4$, 5 vol % O$_2$, and balance gas N$_2$ at a space velocity of 60 000 mL/(g·h). To explore the interaction between CO and CH$_4$ during the catalytic reaction process, the reaction gas composition containing 2 vol % CO, 2 vol % CH$_4$, 5 vol % O$_2$, and balance gas N$_2$ is also tested. Moreover, the catalytic performance of simulated flue gas of the power plant is also assessed, including 2 vol % CO, 2 vol % CH$_4$, 5 vol % O$_2$, 15 vol % CO$_2$, and balance gas N$_2$. The mixture flow rate and space velocity of all the catalytic combustion tests are 100 mL/min and 60 000 mL/(g·h), respectively. The 10 vol % water vapor is also introduced into the simulated flue gas to research the water resistance of the catalyst. The product and reactant of outlet gas is analyzed by the online mass spectrometer HPR-20 Hiden. The detailed experimental setup is exhibited in Figure 2. The conversion X of CO or CH$_4$ is calculated by the equation:

$$X_{CO} = \frac{[CO]_{inlet} - [CO]_{outlet}}{[CO]_{inlet}} \tag{2}$$

$$X_{CH_4} = \frac{[CH_4]_{inlet} - [CH_4]_{outlet}}{[CH_4]_{inlet}} \tag{3}$$

where $[i]_{outlet}$ and $[i]_{inlet}$ are the outlet and inlet concentrations of the reactant i (CO or CH$_4$), respectively.

The reaction rate per unit surface area of the as-prepared catalyst, r_s, is evaluated by the following formula:

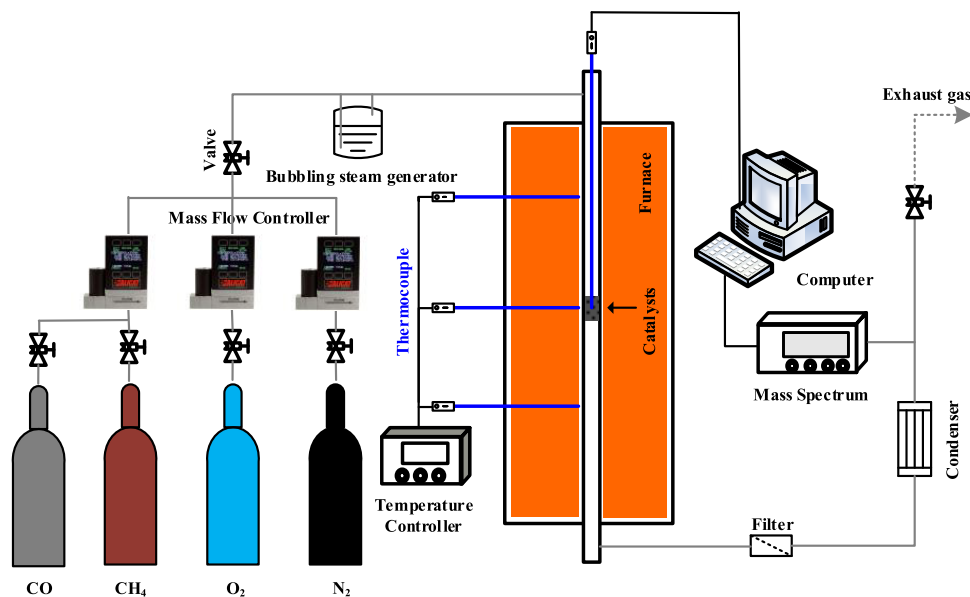$$r_s = \frac{X \times V}{SSA \times 22.4} \tag{4}$$

Figure 2. Experimental setup for catalytic combustion.

Table 2. XRD and BET Data for the CMT Catalysts

catalyst	SSA (m²/g)	BET equivalent diameter d_{BET}(nm)[a]	crystal size (nm)[b]			crystal content (wt %)[c]		crystallinity (%)[d]
			anatase	rutile	Mn_2O_3	anatase	rutile	
4CMT	92.97	16.2	14.34	14.51		61.1	38.9	91.63
12CMT	63.69	21.5	14.86	10.53		9.5	90.5	83.52
20CMT	61.92	21.9	10.35	8.47	7.68	14.2	85.8	70.34
30CMT	61.91	21.1	10.06	5.61	5.77	33.9	66.1	56.75

[a]Evaluated by the equation $d_{BET} = 6/(S \times \rho)$, where S is the specific surface area and ρ is the particle density. [b]Scherrer equation. [c]Determined by the formula $W_{rutile} = (1 + 0.8 \times I_A/I_R)^{-1}$, where I_R and I_A are the intensity of the main diffraction peaks of rutile and anatase, respectively. [d]Determined by the equation $X = \sum I_c/(\sum I_c + \sum I_a)$, where $\sum I_a$ is the scattering integral intensity of the amorphous ingredient, while $\sum I_c$ is the integral intensity of crystal diffraction of the crystalline ingredient.[27]

where X is the conversion percentage, V is the volume flow rate, and SSA is the specific surface area of the catalysts. In addition, T_{50} and T_{90} as indicators of catalytic performance in Table 4 are the temperatures required for 50 or 90% conversion, respectively.

Table 3. Surface Element Compositions for the Cu−Mn/TiO₂ Catalysts

catalyst	binding energy (eV)			Cu^{1+}/Cu	Mn^{4+}/Mn	O_{ads}/O
	Ti $2p_{3/2}$	Cu $2p_{3/2}$	Mn $2p_{3/2}$			
4CMT	458.71	932.87	641.74	0.71	0.55	0.14
12CMT	458.68	932.54	641.97	0.36	0.53	0.23
20CMT	458.58	932.51	641.88	0.26	0.50	0.20
30CMT	458.54	932.58	641.51	0.23	0.39	0.31

3. RESULTS AND DISCUSSION

3.1. Catalyst Structural Characterization. As shown in Table 2, with the rising molar ratio of the Cu−Mn, the specific surface area (SSA) of the CMT catalysts declines from 92.97 m²/g of 4CMT to 61.91 m²/g of 30CMT, with a decrease of 33.4%. The reason is that the increasing content of the transition-metal dopants like CuO_x and MnO_x in the catalyst is more prone to sintering, which has been reported in other researchers' results.[25,26] The BET equivalent diameter of all the catalysts is about 21 nm, except that for the smaller of 4CMT catalysts, which is about 16 nm.

Figure 3a illustrates that the diffraction peak in XRD mainly belongs to rutile phase [PDF-ICDD 21-1276] and anatase phase [PDF-ICDD 21-1272] with the main peaks at $2\theta = 27.4°$ (110) and 25.3° (101), respectively. As the molar concentration of Cu−Mn rises from 4 to 12 mol %, the content of the anatase phase decreases from 61.1 to 9.5 wt %, while that of the rutile phase increases from 38.9 to 90.5 wt %. It indicates the phase transformation from the anatase phase to rutile phase in the synthesis process. Conversely, when the molar content of Cu−Mn increases from 12 to 30 mol %, the content of anatase rises from 9.5 to 33.9 wt %, and the content of rutile decreases from 90.5 to 66.1 wt %. The diffraction peak

of CuO [PDF-ICDD 48-1548] is not observed in the XRD, indicating the highly dispersed copper species on TiO₂, or the small CuO grains formed by FSP. For the 20CMT and 30CMT catalysts, a characteristic peak of the Mn_2O_3 phase [PDF-ICDD 41-1442] appears at $2\theta = 32.9°$. Generally, when the manganese loading is above 6.3 wt %, the XRD peak of large particles Mn_2O_3 can be detected.[28] When the Cu−Mn loading exceeds 12 mol %, the insufficient oxygen and combustion heat provided by organic precursors leads to the reduction of the Mn valence state. Hence, both the Mn_3O_4 and MnO_2 compounds tend to convert to the most stable Mn_2O_3 phase that continuously increases in the product to eventually form the large crystalline grains.

As shown in Figure 3b, with the increase of the Cu−Mn loading, the intensity of the TiO₂ diffraction peak declines, suggesting the decrease of the crystallinity and the growth of amorphous species due to insufficient combustion enthalpy of precursors. In Table 2, the crystallinity has been calculated through Jade software to assess the crystalline and the amorphous phases of Cu−Mn/TiO₂. The crystallinities of 4CMT, 12CMT, 20CMT, and 30CMT are 93, 85, 70, and 54%, respectively. The crystal quality should be further improved especially for highly loaded catalysts (e.g., 20CMT and 30CMT) via regulating flame configurations and/or precursor formulations, which can be considered as future work. Furthermore, the main diffraction peaks of the rutile and anatase phase of the four catalysts are all shifted to a certain degree, caused by Cu and Mn metal ions entering the TiO₂ lattice and forming a solid solution.[29,30] Thus, the increasing molar content of the Cu−Mn promotes the doping and substitution of Cu and Mn ions in the TiO₂, resulting in a reduction of the Cu^{2+} and Mn^{4+} and formation of the oxygen vacancy.[31] In addition, the existence of oxygen vacancies accelerates the diffusion of oxygen ions, which increases the TiO₂ sintering rate and then results in larger particle sizes. The $Ti_nO_{2n−1}$, a secondary intermediate during the oxygen vacancy formation process, provides the nucleation center for the sharp transformation of the anatase phase to the rutile phase between 4CMT and 12CMT.[32] However, when the Cu−Mn content

Table 4. Catalytic Combustion Data Measured for CMT Catalysts

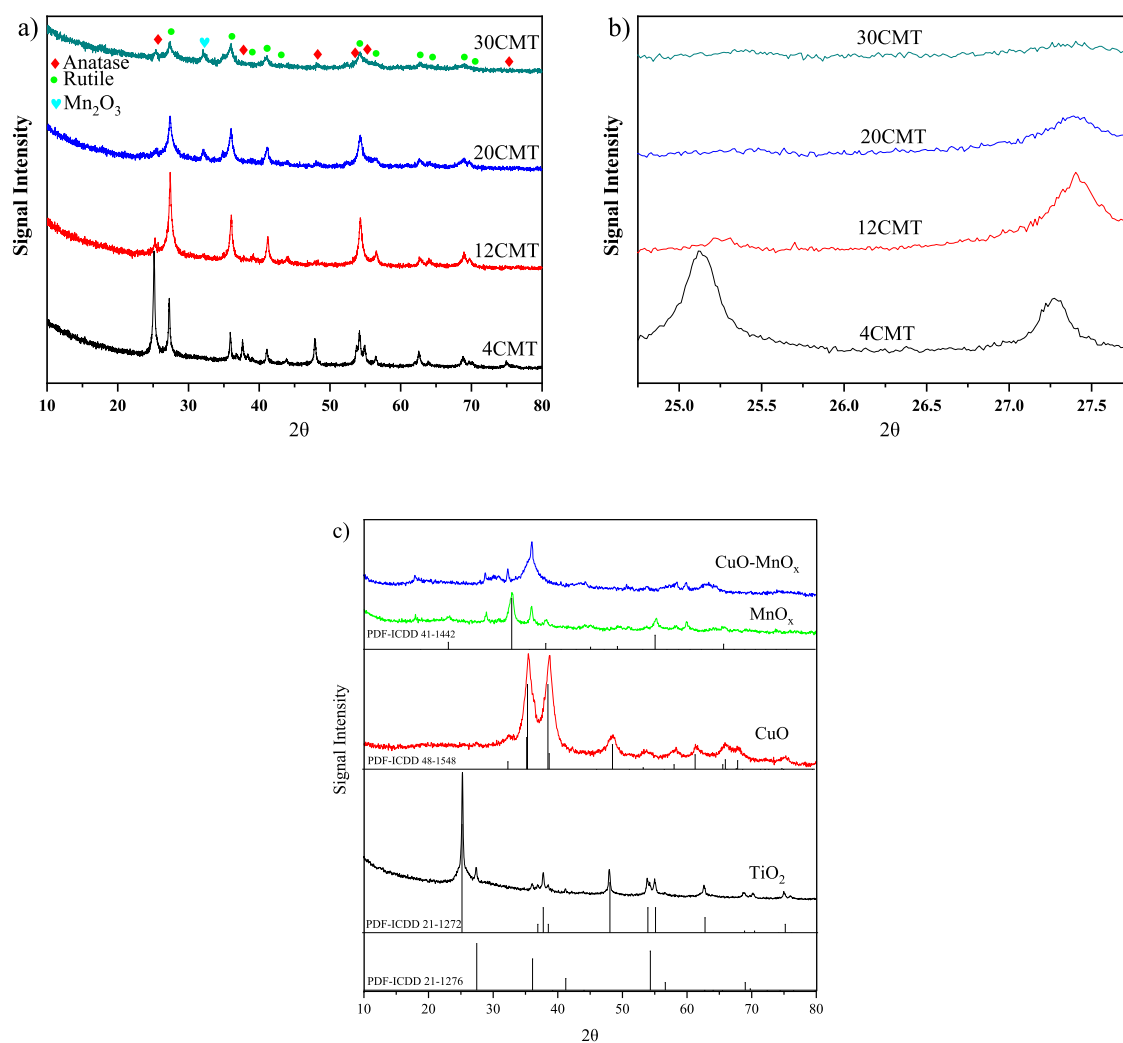| catalyst	CO oxidation			CH₄ oxidation	
	T_{50} (°C)	T_{90} (°C)	r_s at 100 °C (mol·m⁻²·s⁻¹·10⁻⁸)	T_{50} (°C)	r_s at 600 °C (mol·m⁻²·s⁻¹·10⁻⁸)
4CMT	141	168	0.14	550	1.01
12CMT	73	94	2.33	508	1.85
20CMT	90	108	2.02	519	1.64
30CMT	126	137	1.73	538	1.60

Figure 3. XRD patterns of the CMT, TiO_2, CuO, MnO_x, 12CMT, and $CuO-MnO_x$ catalysts.
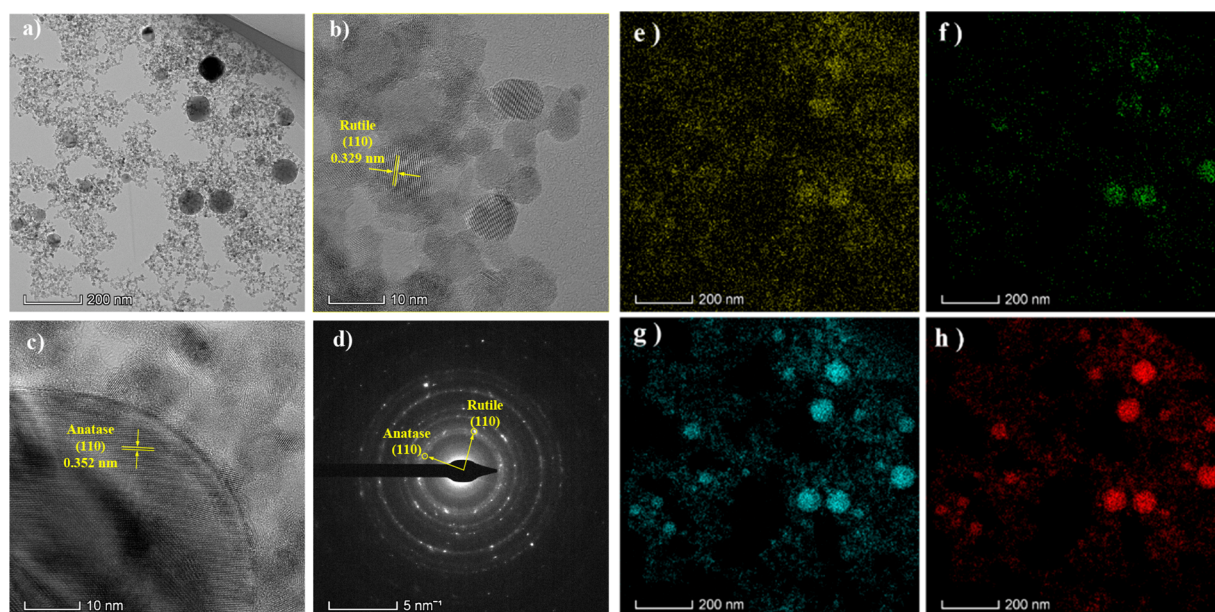

Figure 4. TEM and EDXs of 12CMT catalyst: (a) overall, (b, c) partial selection, (d) SAED, (e) Cu, (f) Mn, (g) O, and (h) Ti.
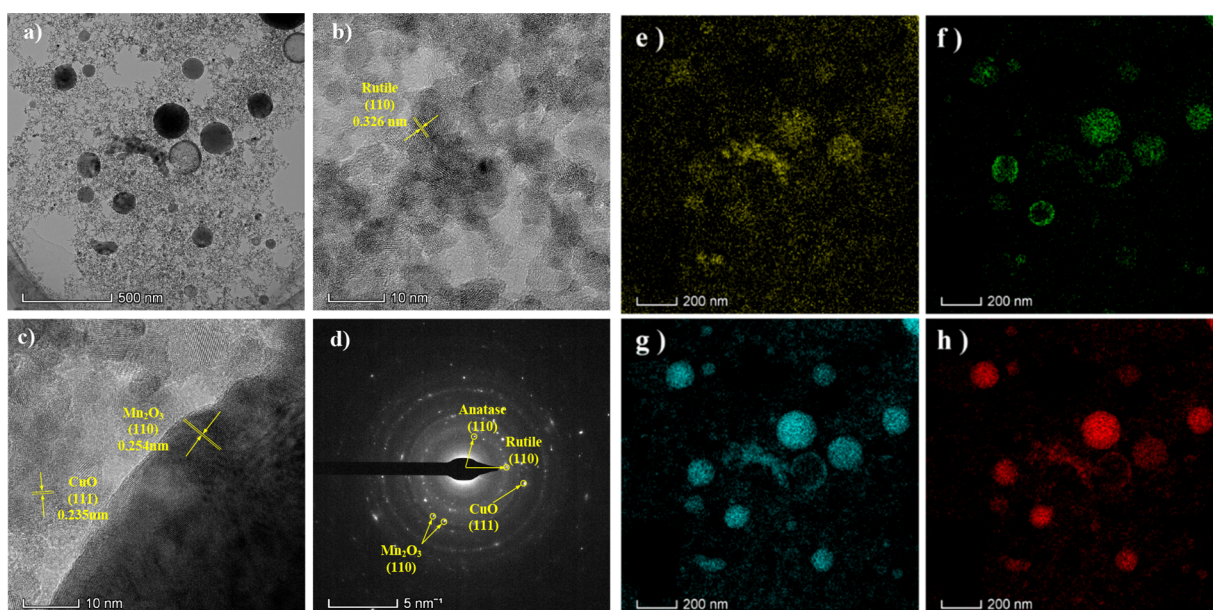
Figure 5. TEM and EDXs of 30CMT catalyst: (a) overall, (b, c) partial selection, (d) SAED, (e) Cu, (f) Mn, (g) O, and (h) Ti.
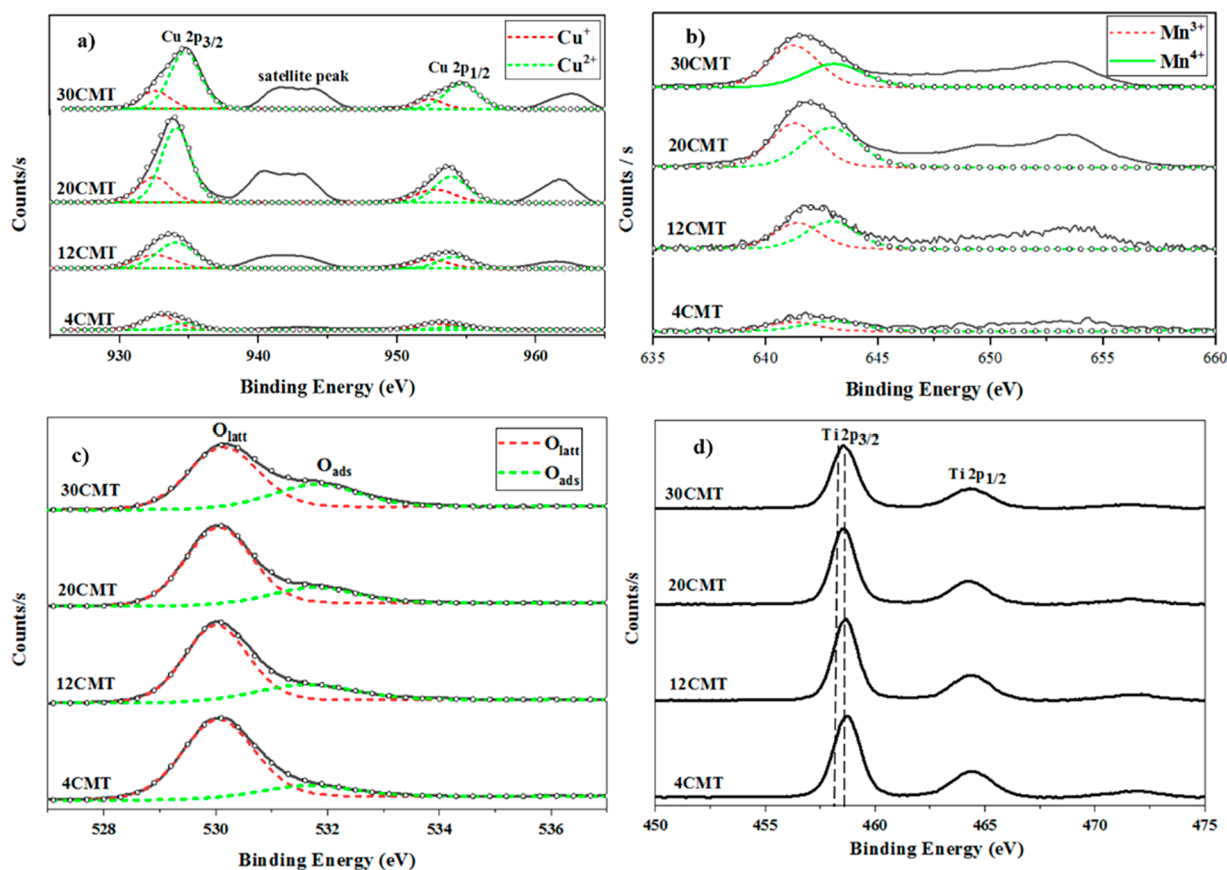

Figure 6. XPS spectra of the Cu−Mn/TiO$_2$ catalysts: (a) Cu, (b) Mn, (c) O, and (d) Ti.

surpasses 12 mol %, the rutile phase decreases from 90.5 to 66.1%. It is inferred that the copper and manganese species could not be incorporated into the TiO$_2$ lattice any more at higher 12 mol % loadings, which suppresses the vacancy concentration.[4]

In Figure 4a, the particle morphology of 12CMT nano-catalyst can be divided into two types: large particles with a

size of 50−100 nm and small particles with a size of 5−10 nm accounting for the majority. However, there are three types of particle morphology of 30CMT catalyst in Figure 5a, the majority of which are small particles at 5−10 nm, which is the same for those of 12CMT, some of which are large particles at 50−200 nm, and a few particles forming the hollow spherical structure. The presence of the inhomogeneous particles has

also been observed in other materials synthesized via FSP.[33−35] Fine particles about 10 nm are obtained by the gas-to-particle conversion through the evaporation of the precursor, nucleation of the gas-phase precursor, and particle growth. On the contrary, the 50−100 nm larger grains generally arise from the droplet-to-particle routes, which is a typical particle formation process by utilization of low-enthalpy precursors, such as copper(II) acetate and manganese acetate. With the rising dopant of Cu−Mn, the overall boiling point of the precursor solution increases. However, the inadequate combustion heat provided by the solvent could not completely evaporate the metal precursors, which thus precipitates on the surface of the droplet to finally form a shell and hollow-sphere particles.[36] The lattice spacing of the rutile (110) crystal plane is 0.329 nm in Figure 4b and 0.326 nm in Figure 5b, which is slightly deviated from the standard value of 0.325 nm. It may be ascribed to the dopant of Cu and Mn metal ions into the TiO₂ lattice. In Figure 5b,c), the small discrete CuO grains less than 4 nm and large Mn_2O_3 particles about 10 nm are found in 30CMT. Additionally, some amorphous substances are distributed around rutile particles in Figure 4b, which may be amorphous CuO_x, MnO_x, etc.

In Figure 4e−h and Figure 5e−h, the EDX analysis is also performed on 12CMT and 30CMT catalysts to further investigate the element distribution of particles. It is seen from Figures 4e and 5e that the Cu element is highly dispersed no matter if it is on the small particles of about 5−10 nm or the large particles of about 50−200 nm, confirming that the very small grain size of copper species is not detected in XRD analysis.[37] In the traditional preparation methods, such as the sol−gel method or impregnation method, the large CuO crystals appear on the carrier as the CuO loading exceeds 12 or 8 wt %, respectively.[38] In this experiment, even though the molar content of Cu−Mn reaches 30 mol % (Cu accounts for 15 mol %), there is still no large crystal of CuO. It indicates that the FSP method is expected to markedly break through the copper loading threshold of the traditional preparation method. As shown in Figures 4e and 5f, the Mn element is prone to gathering around the TiO₂ sphere in comparison with the Cu element. It is deduced that, due to the different ion radii, Cu ions are inclined to embed into the TiO₂ lattice, whereas Mn ions usually replace Ti atoms in supports.

3.2. Cu−Mn/TiO₂ Interaction and Reducibility. Figure 6a illustrates that the binding energy of Cu 2p$_{1/2}$ is at 950−955 eV, and the binding energy of the satellite peak is 938−946 eV. The binding energy of Cu 2p$_{3/2}$ on the CMT is at 913−935 eV, higher than that of bulk CuO and Cu₂O materials. It indicates a stronger interaction between the copper oxide and the TiO₂ support.[4] The peaks of Cu²⁺ and Cu¹⁺ electron binding energies are located at 934 and 932.9 eV, respectively.[24] The appearance of the Cu₂O results from the way CuO decomposes under an oxygen-deficient high-temperature condition as well as the reduction of Cu²⁺ ion by Ti³⁺ and Mn³⁺.[4,39] The strength of the satellite peak as an indicator for Cu²⁺ implies that the most copper element on the surface of 4CMT presents in the form of Cu¹⁺. With the increase of the Cu−Mn molar ratio, the Cu¹⁺/Cu ratio gradually decreases from 0.71 to 0.23 in Table 3, which is a synergistic effect between the redox reaction (Ti⁴⁺ + Cu¹⁺ → Ti³⁺ + Cu²⁺) and the Cu−O−Ti bond.[24,40] This change of the Cu valence state is a crucial characteristic of multivalence cation doping in TiO₂.

In Figure 6b, the electron binding energies of 641.4 and 642.7 eV correspond to the peaks of Mn³⁺ and Mn⁴⁺, respectively.[39] With the increase of the Cu−Mn molar ratio, the Mn⁴⁺/Mn ratio gradually decreases from 0.55 to 0.39 in Table 4. The opposite trend of valence change between copper and manganese elements is attributed to the electron transfer through the reaction Mn⁴⁺ + Cu¹⁺ ↔ Mn³⁺ + Cu²⁺. Furthermore, the reduction of Mn⁴⁺ on the catalyst surface to Mn³⁺ and the formation of the Mn−O−Cu bond promotes the oxidation of CO.[18] However, the decrease of the Mn⁴⁺/Mn ratio also reduces the highly dispersed Mn⁴⁺−O$_{ads}$ Lewis acid−base pairs.[39] Thus, it causes the enrichment of Mn³⁺ on the catalyst surface and, eventually, the occurrence of the large particles of Mn_2O_3 on 20CMT and 30CMT in XRD.

In Figure 6c, the O$_{latt}$ peak at 530.8 eV represents the lattice oxygen, and the O$_{ads}$ peak at 531.7 eV stands for the adsorbed oxygen.[24] As the Cu−Mn molar ratio increases to 12 mol %, more Cu and Mn ions enter into the TiO₂ crystal, which generates more oxygen vacancies on the surface and inside of the TiO₂ carrier as the beneficial defects in oxides. Thus, the bimetal doping effects give rise to a higher amount of adsorption oxygen on the TiO₂ surface. However, the adsorbed oxygen of the 20CMT decreases in comparison with that of 12 mol % samples. The reason is that more Cu and Mn cations than those of 12 mol % are incapable of embedding into the solid solution, resulting in a decreasing content of oxygen vacancy. However, under the 30CMT catalysts, the concentration of the adsorption oxygen remarkably increases. It is attributed to the generation of the surface bimetallic synergetic oxygen vacancies Cu^{x+}−□−Mn^{y+}, forming between Cu and Mn metallic ions on the surface TiO₂.[18] In Figure 6d, the intensity of Ti 2p peaks at 455−470 eV declines by degrees when the Cu−Mn content increases. It implies that the TiO₂ concentration decreases, but the CuO_x and MnO_x are progressively enriched on the CMT surface. Additionally, all the materials exhibit the shift of the Ti 2p$_{3/2}$ binding energy by the doping and substitution of Cu or Mn cations.

The H₂-TPR results of CMT nanocatalysts are shown in Figure 7. The temperatures of the main reduction peak for the four kinds of catalysts with different molar contents are all between 150 and 250 °C. With the addition of the Cu−Mn molar content, H₂ consumption increases from 0.15 mmol/g
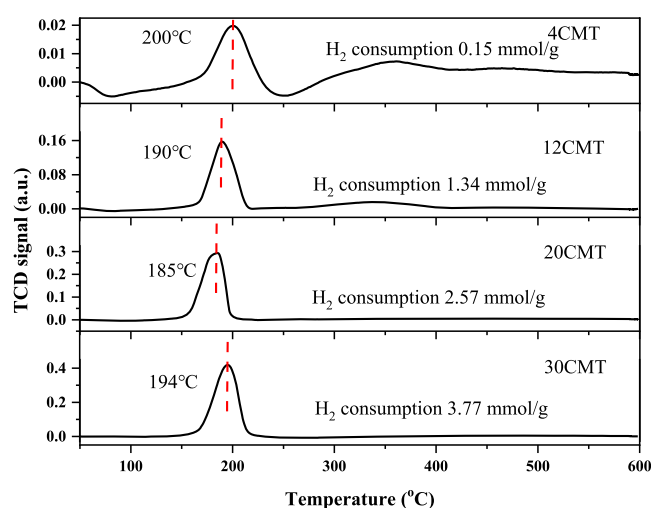

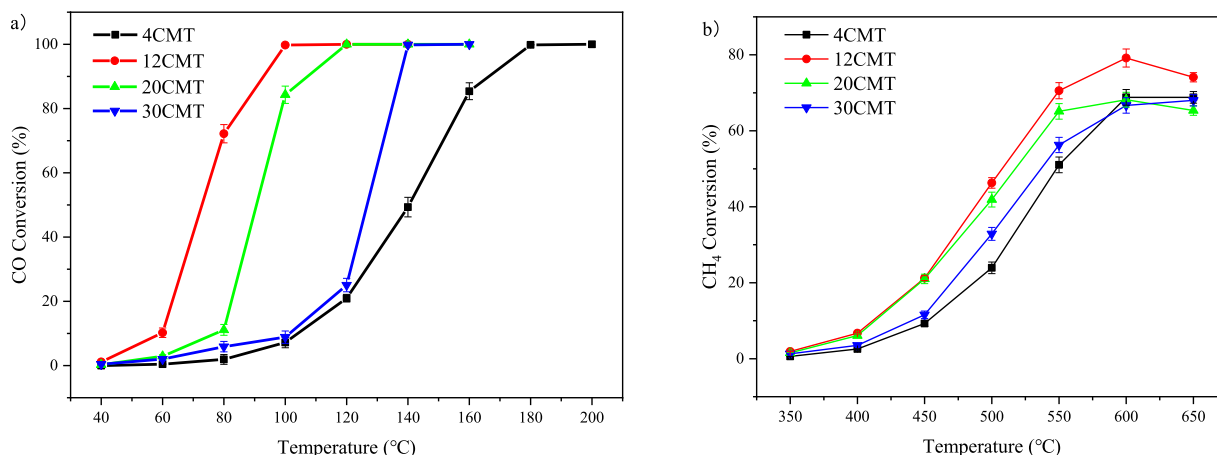**Figure 7.** H₂-TPR profiles for Cu−Mn/TiO₂ samples.

Figure 8. Performance evaluation curves for CO and CH_4 oxidation with $Cu-Mn/TiO_2$ nanoparticles.

Table 5. Comparison of Catalytic Performances for CO or CH_4 Oxidation between the Present Catalysts and Those Reported in Literature Sources

catalyst	preparation method	reaction condition	activity	r_s of CO at 100 °C or CH_4 at 600 °C $(mol·m^{-2}·s^{-1}·10^{-8})$	ref
$Cu-Mn/TiO_2$	FSP	$2\%CO + 5\%O_2 + 93\%N_2$, GHSV = 60 000 mL/(g h)	T_{90} = 94 °C	2.33	this study
$Cu-Mn/TiO_2$	FSP	$2\%CH_4 + 5\%O_2 + 93\%N_2$, GHSV = 60 000 mL/(g h)	T_{50} = 508 °C	1.85	this study
Cu/TiO_2	FSP	$1.5\%CO + 6\%O_2 + 93\%N_2$, GHSV = 60 000 mL/(g h)	T_{90} = 100 °C	1.43	4
$Cu_{1.5}Mn_{1.5}O_4$	FSP	$0.67\%CO + 33.33\%O_2 + 66\%N_2$, GHSV = 40 000 mL/(g h)	T_{90} = 85 °C	0.19	8
$Cu_{0.1}MnO_x$	hydrothermal	$1\%CO + 20\%O_2 + 79\%N_2$, GHSV = 36 000 mL/(g h)	T_{90} = 100 °C	0.36	10
$Cu-Mn/TiO_2-ZrO_2$	hydrothermal	$1\%CO + 21\%O_2 + 78\%N_2$, GHSV = 30 000 mL/(g h)	T_{90} = 170 °C	0.08	43
$6\%Cu/SiO_2$	impregnation	$1.4\%CH_4 + 6\%O_2 + 92.6\%N_2$, GHSV = 30 000 mL/(g h)	T_{50} = 490 °C	0.23	44
$15\%Cu/Al_2O_3$	impregnation	$1.4\%CH_4 + 6\%O_2 + 92.6\%N_2$, GHSV = 30 000 mL/(g h)	T_{50} = 480 °C	0.63	44

4CMT to 3.77 mmol/g 30CMT. As the Cu−Mn loading increases from 4 to 20 mol %, the temperature of the reduction peak instead decreases from 200 to 185 °C. It is known that the H_2-TPR curve of pure MnO_x generally shows two strong reduction peaks at 380 and 480 °C, which are attributed to MnO_2 reduction to Mn_3O_4 and Mn_3O_4 reduction to MnO, respectively.[41] In addition, the hydrogen reduction peak of pure CuO_x is approximately 260 °C.[42] Compared with the bulk CuO_x and MnO_x, the reduction peak temperature of Cu−Mn/TiO_2 nanocatalyst dramatically decreases. When the molar content of the Cu−Mn increases to less than 30 mol %, the temperature of its reduction peak keeps decreasing, due to the hydrogen spillover effect.[4] It is ascribed to highly dispersed Cu and Mn oxides as well as the redox properties of TiO_2 support. Conversely, the temperature reduction peak increases from 20CMT to 30CMT, which results from the decreased dispersion of copper and manganese species and the weakened interaction between Cu−Mn and TiO_2 support, confirming the presence of crystallized Mn_2O_3 and large CuO in Figure 5c. A weak peak appears at 350 °C in 4CMT due to the reduction of the anatase phase. However, when the Cu−Mn loading increases to 12 mol %, the peak slowly decreases and disappears, indicating that the anatase content reduces, and the rutile phase shows less reducibility because of its thermal and structural stability.

3.3. Catalytic Performance and Properties. Figure 8a displays the CO catalytic performance of four kinds of catalysts under various molar loadings with the reaction temperature ranging from 40 to 200 °C. The 12CMT catalyst manifests the optimal catalytic activity for CO, where the ignition point (i.e., the conversion reaches 10%, represented by T_{10}) and 100% conversion are at 60 and 100 °C, respectively. As the Cu−Mn loading constantly increases to 20 and 30 mol %, its performance conversely decreases, such as how the conversions of 20CMT and 30CMT at 100 °C are only 85% and less than 10%, respectively. As shown in Figure 8b, 12CMT also shows the best catalytic performance of CH_4, reaching approximately 80% of conversion at 600 °C. In addition, both 4CMT and 20CMT possess about 68% of conversion at 600 °C; also, 30CMT only reaches 66% of conversion. However, when the reaction temperature further increases to 650 °C, the conversions of all the CMT catalysts even present a slight decrease. In Table4, 12CMT demonstrates the smallest values of both T_{50} and T_{90} for CO oxidation than those of other CMT materials. Additionally, the comparison of catalytic performances for CO or CH_4 oxidation is made between the FSP-synthesized catalysts in this study and those reported in literature sources, as shown in Table 5. For example, the reaction rates of the catalyst surface area (r_s) for CO combustion under 12CMT is evidently higher than 1.43 $mol·m^{-2}·s^{-1}·10^{-8}$ of the FSP-made CuO supported TiO_2
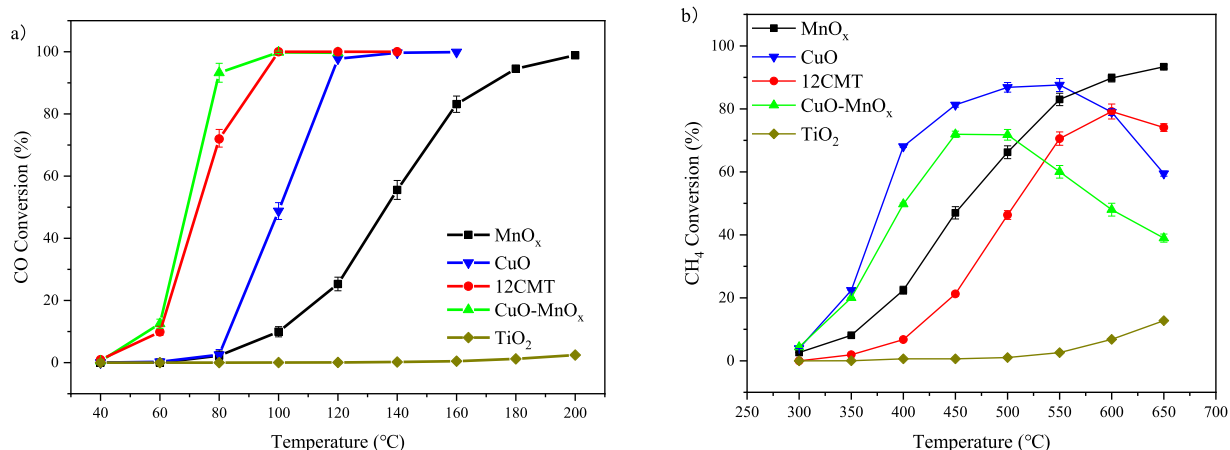
Figure 9. Performance evaluation curves for CO and CH_4 oxidation with TiO_2, CuO, MnO_x, 12CMT, and CuO$-MnO_x$ nanoparticles.

catalysts[4] and 0.19 mol·m^{-2}·s^{-1}·10^{-8} of $Cu_{1.5}Mn_{1.5}O_4$ catalysts.[8]

To further study the effect of each component on catalytic activity, a series of control materials including TiO_2, CuO, MnO_x, and CuO$-MnO_x$ are also made by the FSP protocol for comparison. As shown in Figure 9, the copper oxide presents outstanding catalytic activity below 500 °C, whereas the manganese oxide possesses excellent thermal stability at high temperatures.[1] In addition, the CuO$-MnO_x$ sample exhibits the optimal CO catalytic performance, but the methane oxidation activity decreases sharply when the temperature exceeds 450 °C. On the other side, TiO_2 mainly acts as inert support to enhance the dispersion and sintering resistance of Cu or Mn active components in CMT catalysts.

The CO and CH_4 catalytic performance of the 12CMT nanocatalyst is optimal for the following reasons: (1) The 12 mol % concentration of the dopant is a turning point under four Cu−Mn bimetallic supported catalysts. 12CMT possesses the highest concentration of oxygen vacancy in the TiO_2 lattice, which is responsible for the highest crystal content of the rutile phase. It is known that the copper oxides supported on the anatase surface are reduced with difficulty and manifest the lower catalytic properties for CO combustion.[45] Thus, the increasing ratio of the rutile phase and adsorbed oxygen in CMT plays a pivotal role in the reactive activity. (2) Compared with the large crystalline Mn_2O_3 of 20 and 30 mol % loading, there is not the obvious appearance of the CuO_x and MnO_x phases on the 12CMT nanocatalyst, composed of the largest amount of 5−10 nm small particles. It indicates that the Cu and Mn metal oxides are small and highly dispersed grains, which act as active components for the excellent low-temperature reducibility and catalytic effect. On the other hand, the weaker intensity and wider peak width of the TiO_2 phase on the 20CMT and 30CMT also exert a negative impact on catalytic performance. (3) The larger SSA of 12CMT catalysts can provide more active sites, which is conducive to the adsorption of CO and CH_4 as well as the mass transfer. (4) The synergistic interaction between Cu−Mn and TiO_2 carriers poses a considerable influence on the physicochemical characteristics of CMT. The charge transfer between Cu, Ti, and Mn contributes to the Cu−O−Ti and Mn−O−Cu bond and synergetic oxygen vacancies $Cu^{x+}-\square-Mn^{y+}$, which also explain why the trimetallic Cu−Mn/TiO_2 NPs possess a more outstanding catalytic activity than those of FSP-made bimetallic CuO-TiO_2 and $Cu_{1.5}Mn_{1.5}O_4$ catalysts.

The catalytic combustion of CO, CH_4, (CO + CH_4) mixed gas, and the simulated flue gas of the power plant is carried out with the 12CMT nanocatalyst, as shown in Figure 10. The CO
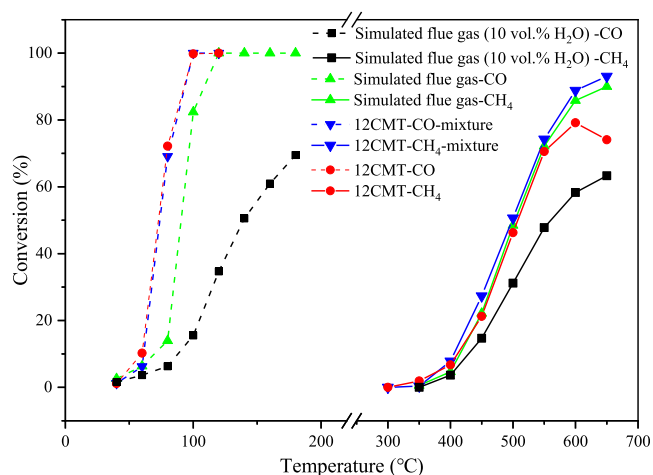

Figure 10. Performance evaluation curves for CO alone or CH_4, CO and CH_4 mixture, simulated flue gas, and water with 12CMT nanoparticle.

catalytic combustion of (CO + CH_4) mixed gas at 12CMT reaches 100% conversion rate at 100 °C, which is the same as that of CO alone, indicating that the existence of CH_4 does not affect the low-temperature catalytic reaction of CO. On the contrary, the CH_4 conversion rate of (CO + CH_4) mixed gas for 12CMT significantly increases from 74 to 93% at 650 °C in comparison with that of CH_4 alone. It is concluded that the heat released from CO combustion at the low temperature could activate the active site on the catalyst TiO_2 carrier to enhance the CH_4 reaction at the high temperature. Compared with that of (CO + CH_4) mixed gas, the CO and CH_4 catalytic performance of 12CMT decreases under the simulated flue gas, whose CO conversion is only 82% at 100 °C. The reason is that the existence of 15 vol % CO_2 promotes backward reactions of CO and CH_4 oxidation.

Under the introduction of 10 vol % H_2O vapor, the CO and CH_4 conversions observably decrease. The conversion of CO is 69% at 180 °C, and the conversion of CH_4 is also decreased to 63% at 650 °C. It is due to the reversible competitive adsorption of water vapor with CO, CH_4, and O_2. In addition,

the negative impact of the water steam at a high temperature is not as great as that at a low temperature. In particular, compared with the commercial hopcalite which is rapidly deactivated in a humid atmosphere, the novel catalysts reveal the significantly modified water vapor stability. A hydrophobization of CMT samples possibly originates from the unburned organic precursors to generate the carbonaceous residues on catalyst surfaces for excellent water resistance.[8]

4. CONCLUSIONS

In this work, the various molar contents of Cu−Mn loading reveal different influences on the structure of the CMT materials and the capacity of CO and CH_4 oxidation combustion. The lattice spacing of TiO_2 is deviated by the incorporation of Cu and Mn cations into the crystal for the generation of oxygen vacancies. It could strengthen the diffusion of oxygen ions to promote the anatase phase and rutile phase transformation. Interestingly, the 12 mol % concentration of dopant is the turning point of chemical−physical characteristics of the Cu−Mn bimetallic supported catalysts. When the Cu−Mn loading exceeds 12 mol % content, no more Cu and Mn species could incorporate into the TiO_2 lattice. Hence, 12CMT possesses the highest crystal percentage of the rutile phase, thanks to the highest concentration of oxygen vacancy in the TiO_2.

The optimum concentration of the Cu−Mn on TiO_2 for catalytic oxidation is 12 mol %. It is ascribed to the component of the highest amount of 5−10 nm small particles and highly dispersed Cu and Mn species. In addition, a higher concentration of the adsorbed oxygen and excellent reducibility of 12CMT also plays a vital role in the catalytic performance, owing to the comprehensive influence of the synergistic effect between Cu−Mn and TiO_2 supports. Moreover, the presence of CO can enhance the catalytic combustion of CH_4 in the $(CO + CH_4)$ mixed gas by activating the active site. In the condition of the simulated flue gas, the existence of CO_2 promotes backward reactions of CO and CH_4 oxidation, causing the reduction of catalytic conversion. Additionally, the CMT catalysts manifest the dramatically modified water vapor stability, which is attributed to a hydrophobization of sample surfaces possibly originating from the unburned organic precursors to generate the carbonaceous residues.

■ AUTHOR INFORMATION

Corresponding Author
   Haibo Zhao − *State Key Laboratory of Coal Combustion, School of Energy and Power Engineering, Huazhong University of Science and Technology, Wuhan 430074, China;* ● orcid.org/0000-0002-2693-4499; Email: hzhao@mail.hust.edu.cn

Authors
   Xing Yuan − *State Key Laboratory of Coal Combustion, School of Energy and Power Engineering, Huazhong University of Science and Technology, Wuhan 430074, China*
   Menglei Qing − *State Key Laboratory of Coal Combustion, School of Energy and Power Engineering, Huazhong University of Science and Technology, Wuhan 430074, China*
   Lingquan Meng − *State Key Laboratory of Coal Combustion, School of Energy and Power Engineering, Huazhong University of Science and Technology, Wuhan 430074, China*

Complete contact information is available at:

https://pubs.acs.org/10.1021/acs.energyfuels.0c02747

Author Contributions
[†]X.Y. and M.Q. contributed to this work equally.

Notes
The authors declare no competing financial interest.

■ ACKNOWLEDGMENTS

■ REFERENCES

(1) Royer, S.; Duprez, D. Catalytic Oxidation of Carbon Monoxide over Transition Metal Oxides. *ChemCatChem* **2011**, *3* (1), 24−65.
(2) He, L.; Fan, Y.; Bellettre, J.; Yue, J.; Luo, L. A review on catalytic methane combustion at low temperatures: Catalysts, mechanisms, reaction conditions and reactor designs. *Renewable Sustainable Energy Rev.* **2020**, *119*, 109589.
(3) Elmhamdi, A.; Castañeda, R.; Kubacka, A.; Pascual, L.; Nahdi, K.; Martínez-Arias, A. Characterization and catalytic properties of $CuO/CeO_2/MgAl_2O_4$ for preferential oxidation of CO in H_2-rich streams. *Appl. Catal., B* **2016**, *188*, 292−304.
(4) Chen, X.; Xu, Z.; Yang, F.; Zhao, H. Flame spray pyrolysis synthesized $CuO-TiO_2$ nanoparticles for catalytic combustion of lean CO. *Proceedings of the Combustion Institute* **2018**, 1.
(5) Wang, Y. X.; Li, D. Y.; Li, K. Z.; Farrauto, R. Enhanced propane and carbon monoxide oxidation activity by structural interactions of CeO_2 with MnO_x/Nb_2O_{5-x} catalysts. *Applied Catalysis B: Environmental* **2020**, *267*, 1 DOI: 10.1016/j.apcatb.2019.118363.
(6) Guczi, L.; Boskovic, G.; Kiss, E. Bimetallic Cobalt Based Catalysts. *Catal. Rev.: Sci. Eng.* **2010**, *52* (2), 133−203.
(7) Wang, D.; Astruc, D. The recent development of efficient Earth-abundant transition-metal nanocatalysts. *Chem. Soc. Rev.* **2017**, *46* (3), 816−854.
(8) Biemelt, T.; Wegner, K.; Teichert, J.; Lohe, M. R.; Martin, J.; Grothe, J.; Kaskel, S. Hopcalite nanoparticle catalysts with high water vapour stability for catalytic oxidation of carbon monoxide. *Appl. Catal., B* **2016**, *184*, 208−215.
(9) Chen, H.; Wang, J.; Li, H.; Wu, D.; Yao, M.; Li, Y. Low temperature combustion of ethylene in a carbon dioxide stream over a cordierite monolith-supported Cu-Mn Hopcalite catalyst. *Appl. Catal., A* **2012**, *427−428*, 73−78.
(10) Gao, J.; Jia, C.; Zhang, L.; Wang, H.; Yang, Y.; Hung, S.-F.; Hsu, Y.-Y.; Liu, B. Tuning chemical bonding of MnO_2 through transition-metal doping for enhanced CO oxidation. *J. Catal.* **2016**, *341*, 82−90.
(11) Biswas, S.; Mullick, K.; Chen, S.-Y.; Kriz, D. A.; Shakil, M. D.; Kuo, C.-H.; Angeles-Boza, A. M.; Rossi, A. R.; Suib, S. L. Mesoporous Copper/Manganese Oxide Catalyzed Coupling of Alkynes: Evidence for Synergistic Cooperative Catalysis. *ACS Catal.* **2016**, *6* (8), 5069−5080.
(12) van Deelen, T. W.; Hernández Mejía, C.; de Jong, K. P. Control of metal-support interactions in heterogeneous catalysts to enhance activity and selectivity. *Nature Catalysis* **2019**, *2* (11), 955−970.
(13) Fujiwara, K.; Okuyama, K.; Pratsinis, S. E. Metal-support interactions in catalysts for environmental remediation. *Environ. Sci.: Nano* **2017**, *4* (11), 2076−2092.
(14) Nguyen, H. M.; Pham, G. H.; Tade, M.; Phan, C.; Vagnoni, R.; Liu, S. Microwave-Assisted Dry and Bi-reforming of Methane over M-Mo/TiO_2 (M = Co, Cu) Bimetallic Catalysts. *Energy Fuels* **2020**, *34* (6), 7284−7294.
(15) Khan, A. A.; Tahir, M.; Bafaqeer, A. Constructing a Stable 2D Layered Ti_3C_2 MXene Cocatalyst-Assisted $TiO_2/g-C_3N_4/Ti_3C_2$

Heterojunction for Tailoring Photocatalytic Bireforming of Methane under Visible Light. *Energy Fuels* **2020**, *34*, 9810.

(16) Morales, F.; de Smit, E.; de Groot, F. M. F.; Visser, T.; Weckhuysen, B. M. Effects of manganese oxide promoter on the CO and H₂ adsorption properties of titania-supported cobalt Fischer–Tropsch catalysts. *J. Catal.* **2007**, *246* (1), 91–99.

(17) Min, H.; Ran, X.; Fan, J.; Sun, Y.; Yang, J.; Teng, W.; Zhang, W.-x.; Li, G.; Zhao, D. Preparation of a mesoporous Cu-Mn/TiO₂ composite for the degradation of Acid Red 1. *J. Mater. Chem. A* **2015**, *3* (14), 7399–7405.

(18) Sun, C.; Tang, Y.; Gao, F.; Sun, J.; Ma, K.; Tang, C.; Dong, L. Effects of different manganese precursors as promoters on catalytic performance of CuO-MnOₓ/TiO₂ catalysts for NO removal by CO. *Phys. Chem. Chem. Phys.* **2015**, *17* (24), 15996–6006.

(19) Li, S.; Ren, Y.; Biswas, P.; Tse, S. D. Flame aerosol synthesis of nanostructured materials and functional devices: Processing, modeling, and diagnostics. *Prog. Energy Combust. Sci.* **2016**, *55*, 1–59.

(20) Singer, C.; Kureti, S. Soot oxidation in diesel exhaust on manganese oxide catalyst prepared by flame spray pyrolysis. *Appl. Catal., B* **2020**, *272*, 118961.

(21) Abe, Y.; Laine, R. M. Photocatalytic La₄Ti₃O₁₂ nanoparticles fabricated by liquid-feed flame spray pyrolysis. *Ceram. Int.* **2020**, *46* (11), 18656–18660.

(22) Li, H. P.; Pokhrel, S.; Schowalter, M.; Rosenauer, A.; Kiefer, J.; Madler, L. The gas-phase formation of tin dioxide nanoparticles in single droplet combustion and flame spray pyrolysis. *Combust. Flame* **2020**, *215*, 389–400.

(23) Mädler, L.; Kammler, H.; Mueller, R.; Pratsinis, S. E. Controlled synthesis of nanostructured particles by flame spray pyrolysis. *J. Aerosol Sci.* **2002**, *33* (2), 369–389.

(24) Meng, L. Q.; Zhao, H. B. Low-temperature complete removal of toluene over highly active nanoparticles CuO-TiO₂ synthesized via flame spray pyrolysis. *Appl. Catal., B* **2020**, *264*, 118427.

(25) Kydd, R.; Teoh, W. Y.; Wong, K.; Wang, Y.; Scott, J.; Zeng, Q. H.; Yu, A. B.; Zou, J.; Amal, R. Flame-Synthesized Ceria-Supported Copper Dimers for Preferential Oxidation of CO. *Adv. Funct. Mater.* **2009**, *19* (3), 369–377.

(26) Davó-Quiñonero, A.; Navlani-García, M.; Lozano-Castelló, D.; Bueno-López, A.; Anderson, J. A. Role of hydroxyl groups in the preferential oxidation of CO over copper oxide-cerium oxide catalysts. *ACS Catal.* **2016**, *6* (3), 1723–1731.

(27) Zheng, B.; Luo, Y.; Liao, H.; Zhang, C. Investigation of the crystallinity of suspension plasma sprayed hydroxyapatite coatings. *J. Eur. Ceram. Soc.* **2017**, *37* (15), 5017–5021.

(28) Liu, Y.; Luo, M.; Wei, Z.; Xin, Q.; Ying, P.; Li, C. Catalytic oxidation of chlorobenzene on supported manganese oxide catalysts. *Appl. Catal., B* **2001**, *29* (1), 61–67.

(29) Inturi, S. N. R.; Boningari, T.; Suidan, M.; Smirniotis, P. G. Visible-light-induced photodegradation of gas phase acetonitrile using aerosol-made transition metal (V, Cr, Fe, Co, Mn, Mo, Ni, Cu, Y, Ce, and Zr) doped TiO₂. *Appl. Catal., B* **2014**, *144*, 333–342.

(30) Barbato, P. S.; Colussi, S.; Di Benedetto, A.; Landi, G.; Lisi, L.; Llorca, J.; Trovarelli, A. Origin of high activity and selectivity of CuO/CeO₂ catalysts prepared by solution combustion synthesis in CO-PROX reaction. *J. Phys. Chem. C* **2016**, *120* (24), 13039–13048.

(31) Hanaor, D. A.; Sorrell, C. C. Review of the anatase to rutile phase transformation. *J. Mater. Sci.* **2011**, *46* (4), 855–874.

(32) Shannon, R. D.; Pask, J. A. Kinetics of the anatase-rutile transformation. *J. Am. Ceram. Soc.* **1965**, *48* (8), 391–398.

(33) Teoh, W. Y.; Amal, R.; Mädler, L. Flame spray pyrolysis: An enabling technology for nanoparticles design and fabrication. *Nanoscale* **2010**, *2* (8), 1324–1347.

(34) Strobel, R.; Pratsinis, S. E. Effect of solvent composition on oxide morphology during flame spray pyrolysis of metal nitrates. *Phys. Chem. Chem. Phys.* **2011**, *13* (20), 9246–9252.

(35) Rudin, T.; Wegner, K.; Pratsinis, S. E. Uniform nanoparticles by flame-assisted spray pyrolysis (FASP) of low cost precursors. *J. Nanopart. Res.* **2011**, *13* (7), 2715–2725.

(36) Jossen, R.; Pratsinis, S. E.; Stark, W. J.; Mädler, L. Criteria for Flame-Spray Synthesis of Hollow, Shell-Like, or Inhomogeneous Oxides. *J. Am. Ceram. Soc.* **2005**, *88* (6), 1388–1393.

(37) He, C.; Yu, Y.; Yue, L.; Qiao, N.; Li, J.; Shen, Q.; Yu, W.; Chen, J.; Hao, Z. Low-temperature removal of toluene and propanal over highly active mesoporous CuCeOₓ catalysts synthesized via a simple self-precipitation protocol. *Appl. Catal., B* **2014**, *147*, 156–166.

(38) Xu, B.; Dong, L.; Chen, Y. Influence of CuO loading on dispersion and reduction behavior of CuO/TiO₂ (anatase) system. *J. Chem. Soc., Faraday Trans.* **1998**, *94* (13), 1905–1909.

(39) Tang, W.; Wu, X.; Li, S.; Shan, X.; Liu, G.; Chen, Y. Co-nanocasting synthesis of mesoporous Cu-Mn composite oxides and their promoted catalytic activities for gaseous benzene removal. *Appl. Catal., B* **2015**, *162*, 110–121.

(40) Deng, C.; Li, B.; Dong, L.; Zhang, F.; Fan, M.; Jin, G.; Gao, J.; Gao, L.; Zhang, F.; Zhou, X. NO reduction by CO over CuO supported on CeO₂-doped TiO₂: the effect of the amount of a few CeO₂. *Phys. Chem. Chem. Phys.* **2015**, *17* (24), 16092–109.

(41) Xingyi, W.; Qian, K.; Dao, L. Catalytic combustion of chlorobenzene over MnOₓ-CeO₂ mixed oxide catalysts. *Appl. Catal., B* **2009**, *86* (3–4), 166–175.

(42) Morales, M. R.; Barbero, B. P.; Cadús, L. E. Total oxidation of ethanol and propane over Mn-Cu mixed oxide catalysts. *Appl. Catal., B* **2006**, *67* (3–4), 229–236.

(43) Gong, Y.; Chen, H.; Chen, Y.; Cui, X.; Zhu, Y.; Zhou, X.; Shi, J. A Cu/Mn co-loaded mesoporous ZrO₂-TiO₂ composite and its CO catalytic oxidation property. *Microporous Mesoporous Mater.* **2013**, *173*, 112–120.

(44) Águila, G.; Gracia, F.; Cortés, J.; Araya, P. Effect of copper species and the presence of reaction products on the activity of methane oxidation on supported CuO catalysts. *Appl. Catal., B* **2008**, *77* (3), 325–338.

(45) Zhu, H.; Wu, Y.; Zhao, X.; Wan, H.; Yang, L.; Hong, J.; Yu, Q.; Dong, L.; Chen, Y.; Jian, C.; et al. Influence of impregnation times on the dispersion of CuO on anatase. *J. Mol. Catal. A: Chem.* **2006**, *243* (1), 24–30.